NANO LETTERS

Letter

pubs.acs.org/NanoLett

Fabrication of High-*Q* Nanobeam Photonic Crystals in Epitaxially Grown 4H-SiC

David O. Bracher*,† and Evelyn L. Hu‡

†Department of Physics and ‡School of Engineering and Applied Sciences, Harvard University, Cambridge, Massachusetts 02138, United States

ABSTRACT: Silicon carbide (SiC) is an intriguing material due to the presence of spin-active point defects in several polytypes, including 4H-SiC. For many quantum information and sensing applications involving such point defects, it is important to couple their emission to high quality optical cavities. Here we present the fabrication of 1D nanobeam photonic crystal cavities (PCC) in 4H-SiC using a dopant-selective etch to undercut a homoepitaxially grown epilayer of p-type 4H-SiC. These are the first PCCs demonstrated in 4H-SiC and show high quality factors (Q) of up to ∼7000 as well as low modal volumes of <0.5 $(\lambda/n)^3$. We take advantage of the high device yield of this fabrication method to characterize hundreds of devices and determine which PCC geometries are optimal. Additionally, we demonstrate two methods to tune the resonant wavelengths of the PCCs over 5 nm without significant degradation of the Q. Lastly, we characterize nanobeam PCCs coupled to luminescence from silicon vacancy point defects (V1, V2) in 4H-SiC. The fundamental modes of two such PCCs are tuned into spectral overlap with the zero phonon line (ZPL) of the V2 center, resulting in an intensity increase of up to 3-fold. These results are important steps on the path to developing 4H-SiC as a platform for quantum information and sensing.

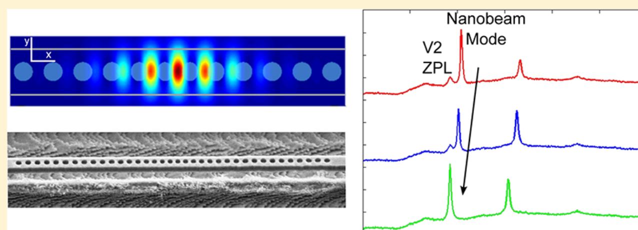

KEYWORDS: *Silicon carbide, point defects, photonic crystal cavities, nanobeam photonic crystals, mode tuning*

There has been much recent interest in point defects in silicon carbide (SiC), which have intriguing single photon and spin properties.[1−5] As with the NV center in diamond, the spin active defects can be used for magnetic field, temperature, and other types of sensing[6,7] as well as quantum information applications.[1,2,8,9] Of particular interest in 4H-SiC are the defect centers related to silicon vacancies[3,4] and to divacancies.[1,9,10] These defects show sharp zero phonon lines (ZPL) with accompanying, broad phonon sidebands. Because the ZPL emission is necessary for many quantum information applications, it is imperative to enhance the emission of the defects into the ZPL. This can be achieved through the use of high-quality photonic cavities.[11−14]

Several groups have demonstrated the ability to fabricate high quality cavities in both 3C- and 6H-SiC, including microdisks,[15−17] microring resonators,[18] and photonic crystal cavities (PCCs).[19−24] Our SiC cavities employ a homoepitaxially grown wafer of 4H-SiC along with a dopant-selective photoelectrochemical (PEC) etch to achieve optical isolation, as has been reported previously.[25] This approach therefore obviates possible effects of strain attendant to the hetero-epitaxial growth of 3C-SiC on Si[26] or defects in the material induced by ion implantation and wafer bonding used to prepare 6H-SiC on insulator.[27] Avoiding these effects helps achieve high quality photonic devices and is likely important for preserving defect properties. The SiC nanobeam cavities reported here have quality factors (Q's) as high as ∼7000 at wavelengths ∼700 nm, which is nearly on par with the highest reported in 6H-SiC[24] (∼10^4) and higher than those demonstrated in 3C-SiC.[19−21] Additionally, ours are the first photonic crystal cavities demonstrated in 4H-SiC, an important step in achieving controllable cavity coupling to the 4H-SiC defects. Moreover, the high yield of high Q cavities possible with this technique provides a good statistical sampling that allows us to choose the best cavity design with the largest process latitude. In addition to fabricating and characterizing the cavities, we demonstrate the ability to controllably tune the cavity resonance over 5 nm without degradation of the cavity Q, which is very important for achieving spectral overlap between defect emission and the cavity mode. Lastly, we use ion implantation to create silicon vacancy centers in fabricated cavities and observe PCC modes decorating the defect center luminescence. Employing the above tuning techniques, we bring the fundamental mode of two separate nanobeam PCCs into spectral overlap with the ZPL of the V2 silicon vacancy center and observe an intensity increase of up to 3 times. To the best of our knowledge, this is the first demonstration of point defects in 4H-SiC coupled to photonic devices.

We chose to fabricate 1D nanobeam PCCs for several reasons. First, the degree of achievable cavity-emitter coupling is significantly influenced by the ratio of Q and modal volume (V) of the cavity.[28] It is therefore crucial to have cavities with high Q and low V to be useful for defect emission

Received: June 26, 2015
Revised: August 17, 2015
Published: August 25, 2015

© 2015 American Chemical Society

DOI: 10.1021/acs.nanolett.5b02542
Nano Lett. 2015, 15, 6202−6207

enhancement. Nanobeam PCCs satisfy these constraints with extremely high theoretical Q values ($>10^6$) and low modal volumes ($<(\lambda/n)^3$).[29] Additionally, the wavelength of the fundamental TE resonance of the nanobeam PCC can be finely controlled by adjusting the device scale. Indeed, given these advantages, nanobeam PCCs have been shown to be promising platforms for achieving Purcell enhancement in other materials, like diamond.[12−14] In addition, the 1D geometry of the nanobeams makes them easier to undercut than a larger 2D photonic crystal structure, providing good optical isolation.

The selected cavity design consists of two sets of equally spaced holes forming Bragg mirrors around a central set of holes. In the central region, the hole size and lattice constant are linearly tapered over a series of holes from the original size in the outer regions down to 84% of that size. By reducing the Fourier components of the cavity fields that can leak out of the cavity, the tapering leads to better confinement of the light in the cavity and is important for maximizing the cavity's theoretical Q.[30] To efficiently optimize our fabrication method, we chose to target the cavity modes to a broadband, visible background luminescence native to our material with a spectral range of approximately 600−800 nm. While the origin of this luminescence is uncertain, it bears some similarity to the point defect emission reported in refs 5 and 31 or may be due to a broad luminescence from bands of defect states as seen both in the related material 3C-SiC[17] and in our epilayer material, Al-doped 4H-SiC.[32] Therefore, our chosen design employed a lattice constant of 200 nm and a beam width of 350 nm, which showed a fundamental TE mode at ∼700 nm according to FDTD simulations (Lumerical Inc.). This base design was used in four specific implementations that vary in the number and the type of holes in the tapered region. Specifically, we used either 4 or 8 holes on each side of the tapered region (with 14 or 10 holes respectively in each Bragg region), and these holes were either circular or elliptical. In the elliptical holes, the tapering is done only along the axis parallel to the beam (x-axis in Figure 1), yielding an eccentricity of 0.54 in the most-tapered elliptical holes. These two parameters combine to give four possible designs. The simulated field profile of the fundamental mode for one such design (eight elliptical holes) can be seen in Figure 1a. The simulated Q of this mode is 5×10^6, and the simulated mode volume is $0.45(\lambda/n)^3$, calculated using the standard cavity QED definition.[33] Similarly, the designs with four elliptical holes and eight circular holes show simulated Q of $\sim 5 \times 10^6$ as well, whereas the design with four circular holes shows simulated Q of 8×10^5. All simulated mode volumes lie in the range of 0.4−0.5 $(\lambda/n)^3$. Lastly, we used the same lattice constant in all designs in order maintain as much similarity in fabrication as possible. However, because the tapering is slightly different in each design, the simulated wavelengths of the fundamental TE mode range from 680 to 700 nm, depending on device geometry.

To fabricate our devices (fabrication schematic shown in Figure 2), we begin with a wafer consisting of an n-type (nitrogen, 10^{19} cm^{-3}) 4H-SiC substrate with a homoepitaxially grown 250 nm p-type epilayer (aluminum, 10^{17} cm^{-3}, epilayer provided by Norstel AB). The bulk wafer was diced into 6 mm squares for fabricating individual samples. To create an ohmic contact for later PEC etching, we deposit 100 nm of nickel by thermal evaporation on the backside (side without the epilayer) of each sample. After deposition, the samples are annealed at 900 C to improve Ni adhesion. A second thermal evaporation

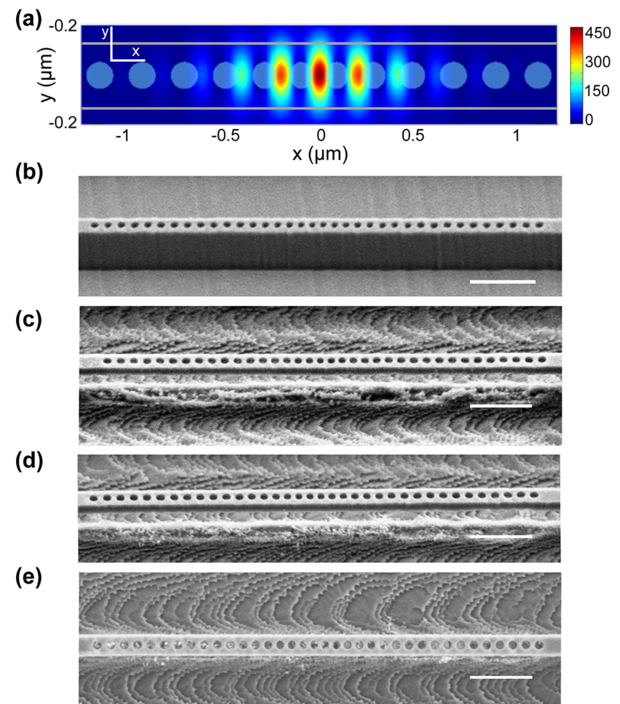

Figure 1. (a) FDTD simulated field intensity profile of fundamental TE mode for 1D nanobeam photonic crystal (PCC). (b) Nanobeam PCC after etching pattern into SiC substrate. The etch depth is 850 nm. (c) Nanobeam PCC after photoelectrochemical etch to remove n-type substrate. The undercut is 600 nm. (d) Nanobeam PCC after annealing at 750 C and dip in buffered oxide etchant. (e) Top-down view of nanobeam PCC. The scalloping seen is on the bottom etched SiC surface and does not affect the quality of the suspended nanobeams. All scale bars indicate 1 μm.

step is then used to deposit 100 nm of aluminum to serve as an etch mask. The desired patterns are then written using electron beam lithography with positive-tone resist (PMMA C6). After being written, the pattern is transferred to the Al layer using chlorine-based reactive ion etching (RIE) (Unaxis Shuttleline) and then from the Al mask to the SiC substrate by a further fluorine-based RIE step (STS ICP-RIE).

Figure 1b shows a side view of an individual nanobeam following SiC etching. Note that, in addition to the line of holes, two 2 μm wide trenches serve to define the beam and allow the substrate to come into ample contact with the KOH solution during PEC etching. The side view shows that the beams are etched 850 nm into the SiC, which allows for sufficient optical isolation of the 250 nm epilayer. To achieve this isolation, we then use the dopant-selective PEC etch process described in ref 25 to remove the n-type substrate beneath the epilayer. The sample is placed in 0.2 M KOH with a 0.2 V applied bias for 16 h, with simultaneous mercury lamp illumination. Figure 1c shows a beam that has been undercut using this process. Due to the nature of the undercut,[25] there are patches of porous n-type SiC substrate beneath the beam, as observed in our previous work using the PEC etching to fabricate microdisks. Because this material may degrade the device quality, we anneal the sample at 750 C for 30 min, which oxidizes the porous remnants. The oxidized material can be removed with standard buffered oxide etchant (BOE), leading to cleaner optical isolation of ∼600 nm (Figure 1d). A top-down view of a nanobeam after all stages of fabrication is shown

DOI: 10.1021/acs.nanolett.5b02542
Nano Lett. 2015, 15, 6202−6207

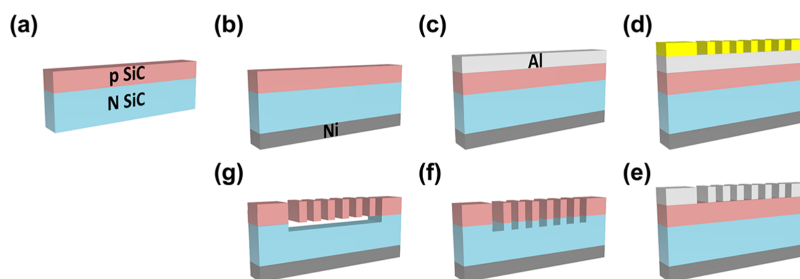

Figure 2. Schematic of fabrication flow. (a) The starting material is a 250 nm epilayer of p-type 4H-SiC homoepitaxially grown on a substrate of n-type 4H-SiC. (b) 100 nm of Ni is thermally evaporated on the backside of each sample. (c) 100 nm of Al is thermally evaporated to serve as an etch mask. (d) Electron beam lithography is used to define the desired pattern in PMMA resist. (e) The pattern is transferred to Al by reactive ion etching (RIE) with a chlorine-based chemistry. (f) The pattern is transferred to SiC by a further fluorine-based RIE step. (g) Dopant-selective photoelectrochemical etching is used to remove the n-type substrate beneath the patterned devices. The sample is annealed at 750 C and dipped in buffered oxide etchant to improve undercut.

in Figure 1e. Additionally, Figure 2 shows a schematic of the entire fabrication process.

To assess the optical properties of the fabricated devices, we performed confocal photoluminescence (PL) spectroscopy with a commercial Raman system (LabRAM ARAMIS, Horiba Jobin-Yvon). Using this system, the nanobeam PCCs were excited with a 532 nm laser. The resultant spectra showed PCC cavity modes decorating a broadband visible background luminescence. Figure 3 shows spectra taken from each of the

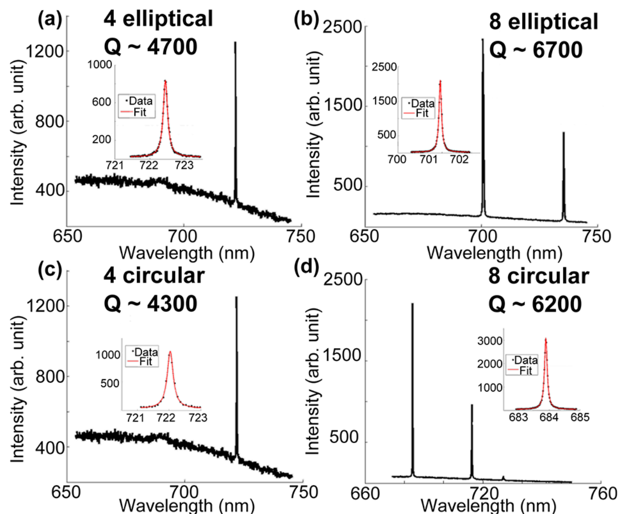

Figure 3. Photoluminescence spectra of the best measured device for each of the four geometries fabricate: (a) four elliptical holes, (b) eight elliptical holes, (c) four circular holes, and (d) eight circular holes. A higher resolution spectrum was taken near resonances. The fundamental TE mode for each spectrum is shown inset, along with a Lorentzian fit.

four device geometries. In each subfigure, the peak corresponding to the fundamental TE mode of the device was fit to a Lorentzian curve (inset) to extract relevant properties of the resonance. We see that we are able achieve high Q factor (>4000) modes with all four geometries, and the best observed device shows a Q factor of nearly 7000. Having simulated the effects on Q of the measured surface roughness of our structures, and of possible absorption due to the p-type doping, we believe that the difference in measured versus theoretical Q is most likely due to fabrication errors, including damage from RIE, deviations in hole positions and sizes, and especially nonverticality of the sidewalls due to imperfect etching.[20,34] We also cannot rule out the possibility of subtle material defects and their absorption of light.[35]

Moreover, the monolithic substrate used allows for the fabrication of hundreds of nanobeam cavities on the same chip which can be simultaneously undercut. These devices therefore have the same fabrication history with the exception of controllable variables like cavity geometry and lithography dose. The spectra of all devices can be acquired and then the properties of the cavity resonances can be easily analyzed en masse with a home-built code. We were thus able to analyze the statistics of PCC resonances (quality factors and resonant wavelengths) for each nanobeam design, fabricated using 5 different electron beam doses ranging from 1300 to 1700 μC/cm^2. This large-scale analysis of the fabricated cavities reveals that more than 80% of the 221 beams studied showed PCC resonances, even over the considerable range of e-beam doses. The lowest doses produced resonances that were red-shifted (730−740 nm) from the designed value, as is reasonable for the resulting smaller diameter hole sizes. The higher doses resulted in average wavelengths closer to 690−700 nm, with a smaller variation in Q values among the four designs.

Table 1 shows the mean Q for each design as well as the percent of devices with Q > 1000. The design with eight

Table 1. Results of Analysis of Primary Resonant Mode of 221 Nanobeams

type	N	mean Q	%Q > 1000	25th−75th percentile Q range	mean λ (nm)	simulated λ (nm)
4c	54	1340	57.4	720−1920	707.5	703.0
4e	56	1280	51.9	670−1610	709.0	700.0
8c	55	1430	58.1	910−1760	698.7	687.5
8e	56	1600	88.9	1040−1780	704.9	684.0

elliptical holes shows a noticeably higher mean Q, as well as a significant advantage in the percentage of devices with Q > 1000. Table 2 shows the analogous data for a dose of 1400 μC/cm^2, which gives mean resonant wavelengths having good agreement with simulations. Again, the 8e design shows a notably higher mean value of Q. This analysis shows that the fabrication method demonstrated here is robust, leading to high device yields and thus the ability to analyze hundreds of devices. The robustness of this method is important in that it allows us to easily study the resonant wavelength differences between simulated and fabricated devices, the effect of electron beam lithography conditions on device quality, and the effect of

DOI: 10.1021/acs.nanolett.5b02542
Nano Lett. 2015, 15, 6202−6207

Table 2. Results of Analysis of Primary Resonant Mode of 53 Nanobeams Fabricated Using Best Electron Beam Lithography Dose (1400 μC/cm^2)

type	N	mean Q	% Q > 1000	mean λ (nm)	simulated λ (nm)
4c	13	1280	54	704.8	703.0
4e	14	1490	50	714	700.0
8c	13	1590	69	699.7	687.5
8e	13	2040	100	709	684.0

different geometries on device quality. Analysis on a further 600 nanobeam cavities has shown that the geometry with eight elliptical holes in the tapered region consistently shows both the highest average Q factor and the highest yield of high Q factor devices. Although the four elliptical, eight elliptical, and eight circular hole designs all show similar Q factors in simulation, there seems to be a measurable difference between these designs upon fabrication. Characterizing these differences helps us optimize cavity design for future devices and shows that the fabrication method is somewhat sensitive to small variations in design.

Because our goal is to eventually match the PCC resonances to the ZPL of the spin-active, IR defects, it is important to be able to precisely tune the resonant wavelength and to do so without severely harming the quality of the device being tuned. We now demonstrate two such tuning methods. The first method uses a gentle RIE process to slowly thin the nanobeam PCCs isotropically, resulting in the progressive blue shifting of the resonances of all devices on the sample. To study this effect, we performed successive steps of etching, taking spectra from a select set of devices after each etch step to determine the new wavelength and quality factor of each resonance. Every etch step consisted of 30 s of exposure to CF_4 plasma at a gas flow of 20 sccm and power of 75 W. Because the whole sample is placed in the RIE reactor, all devices are simultaneously affected. On the other hand, the second type of tuning studied was accomplished by laser irradiating individual devices. In this process, a PCC is exposed to the unattenuated excitation laser (30 mW) described above for 30 s (while taking spectra for device characterization, the laser is attenuated by a factor of 100 to avoid mode tuning or broadening). After irradiation, the resonance is slightly blue-shifted, but further irradiation does not lead to further shift. After being dipped in buffered oxide etchant (BOE) for 1 min, the resonance displays slightly more blue shift but more importantly can again be blue-shifted by further irradiation. We believe that the irradiation drives oxidation at the surface of the device and therefore is self-limiting, as the surface oxidation saturates. The BOE removes this oxide and allows further oxidation. This self-limiting tuning process is similar to "digital etching" previously reported in another material system.[36] This type of digital etching can be very useful for two reasons. First, it allows us to tune the modes of individual devices without affecting other devices on the same chip, which is especially important if we want to simultaneously spectrally match the modes of several devices to defect ZPLs. Additionally, the self-limiting nature of the etch allows us to take small, discrete steps to carefully tune a mode to the desired wavelength, without the risk of overshooting. Finally, this tuning method is simpler and less time-consuming than the RIE process described.

Figure 4a−c and d−f shows the results of the RIE tuning and laser irradiation tuning, respectively, for a selection of the measured beams. Figure 4a and d shows the shift of the absolute wavelengths as a function of the etch step, while Figure 4b and e shows the cumulative change in wavelength for each resonance. Note, for irradiation tuning, a full tuning step consists of irradiation and rinsing in BOE. Finally, Figure 4c and f shows the range of measured quality factors for each device throughout the tuning process—the top bar and bottom bar for each device represent the maximum and minimum Q factor for the given device, respectively. Additionally, the "x" marker indicates the initial Q of the device, and the dot marker represents the Q of the device after all tuning. The RIE tuning shows a mean shift of 0.77 ± 0.14 nm per step, while the laser irradiation tuning shows a mean shift of 0.83 ± 0.25 nm per step. At worst, the minimum Q throughout tuning is ∼20% (and typically less than 10%) lower than the starting Q for both methods, and the mean change in Q from start to finish is negligible; indeed, for both methods the number of devices (including those not shown in Figure 4) that increased in Q from start to finish was equal to the number that decreased. We believe the variation in Q is probably due mainly to a combination of uncertainty in the fit and small variations in the surface of the device throughout the tuning. Therefore, both tuning methods can be used without significant variation in quality of the device. When combined, the two tuning methods offer a powerful way to tune the device resonances—coarse correction of all devices on a given sample by RIE tuning for

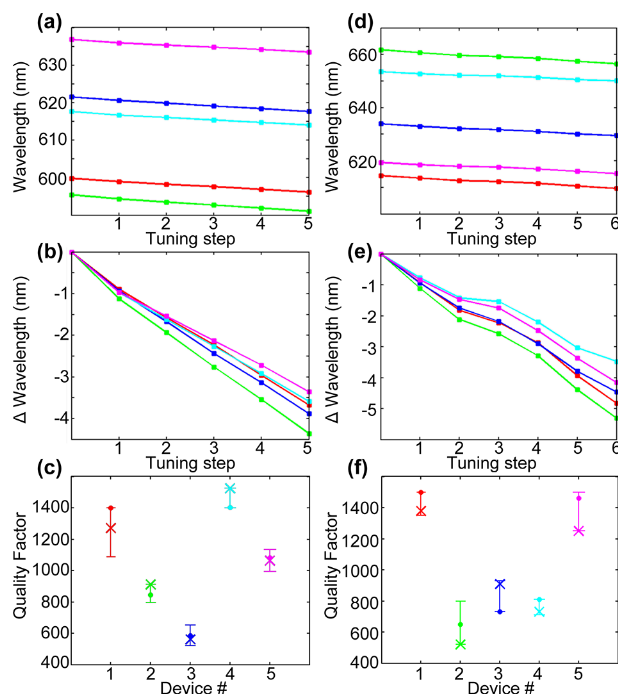

Figure 4. Tuning of nanobeam PCC resonant wavelengths. (a) Absolute wavelength vs tuning step for a selection of devices tuned using RIE in CF_4 plasma. Each step consists of 30 s of etching. (b) Cumulative wavelength change vs tuning step for resonances shown in panel a. (c) Variation of quality factor for each device shown in a,b throughout tuning process. Top bar and bottom bar represent maximum and minimum Q for each device. "x" marker indicates Q before tuning, and dot marker indicates Q after all tuning has been completed. (d) Same as a, but for devices tuned using laser irradiation tuning. Each step consists of laser irradiation for 30 s and a dip in BOE for 1 min. (e,f) Same as b,c for devices tuned using laser irradiation. In a−c and in d−f each color corresponds to the same device in all three plots.

DOI: 10.1021/acs.nanolett.5b02542
Nano Lett. 2015, 15, 6202−6207

the necessary length of time followed by precision tuning of individual PCCs using laser irradiation tuning.

To demonstrate the efficacy of the above fabrication and tuning methods, we also report on nanobeam PCCs coupled to point defects in 4H-SiC. The devices were fabricated as described previously, with two different lattice constants, 290 and 320 nm. FDTD simulations showed fundamental modes with wavelengths of ∼920 nm and ∼1000 nm, respectively, for these devices. The silicon vacancy defect center shows photoluminescence characterized by ZPLs near 860 nm (V1) and 916 nm (V2), corresponding to the two possible defect orientations, with a phonon sideband spanning to at least 1100 nm.[3,4] Consequently, we expected nanobeam PCCs with both lattice constants to exhibit modes decorating the silicon vacancy luminescence. After device fabrication, the samples were ion implanted (CuttingEdge Ions) with 70 keV C_{12} ions at a dose of 10^{13} ions/cm^2, without postannealing. The ion implantation damages the SiC lattice, and among the defects created are the desired silicon vacancies.

After ion implantation, we once again characterized the devices using PL spectroscopy. PL measurements were made at room temperature (∼300 K) using the commercial Raman system, with an excitation wavelength of 785 nm to efficiently pump the silicon vacancy centers. Measurements were also taken at 77 K using a home-built, confocal PL setup. In this setup, a Ti:sapphire laser tuned to 760 nm was used for excitation, and a 1D InGaAs array (Princeton Instruments, working range 800−1700 nm) was used for detection. Figure 5a shows spectra at both 300 and 77 K taken on the implanted, unpatterned substrate to confirm the presence of the defects. The spectra match what has been previously reported,[3,4] and at 77 K, the ZPLs corresponding to both the V1 and V2 centers are visible. Additionally, Figure 5b shows a set of representative spectra (vertically offset for clarity) from several nanobeam PCCs on the implanted samples. These spectra clearly show nanobeam modes decorating the silicon vacancy center luminescence. The upper two spectra (red and blue traces) were taken from devices with 320 nm lattice constant, while the rest were taken from devices with 290 nm lattice constant. Of the ion-implanted PCCs measured, nearly half showed modes with $Q > 1000$, and the highest Q observed was 1900.

To test the capability of our laser irradiation tuning to achieve spectral overlap between a nanobeam mode and a point defect ZPL, we chose two devices with modes slightly red-shifted from the V2 ZPL. These devices were both tuned in steps toward the ZPL using laser irradiation to blue shift the modes. Figure 5c and d shows spectra acquired at 77 K for both devices as the fundamental mode is first near the ZPL and then spectrally overlaps the ZPL. On both PCCs, there are secondary modes that tune along with the fundamental mode but are far from the ZPL. The mode for the device in Figure 5c was measured to have Q of 1100, while that of Figure 5d was measured to be 1000. Moreover, after the mode has been tuned into spectral overlap with the ZPL, the device in Figure 5c shows an intensity increase of slightly greater than 1, and the device in Figure 5d shows a 3-fold intensity increase. Figure 5e shows just the mode and ZPL for two of the spectra in Figure 5d, to better visualize the increase in intensity. FDTD simulations of the far-field radiation pattern of the resonant mode, similar to the analysis in ref 37, indicate that when the mode spectrally overlaps the ZPL, an intensity increase of ∼1.5 times may be due to more light being directed into the 0.5 NA collection objective. Nevertheless, while some of the observed

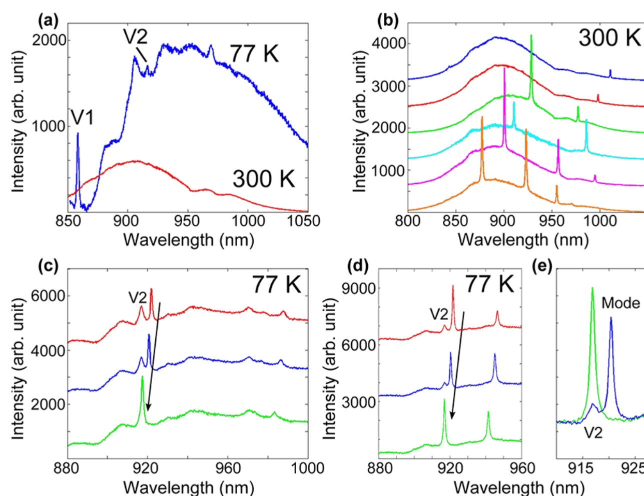

Figure 5. Silicon vacancy centers coupled to nanobeam PCCs. (a) Photoluminescence (PL) spectra of implanted, unpatterned substrate at 300 K (excitation 785 nm) and 77 K (excitation 760 nm). Spectrum at 77 K shows distinct ZPLs for the two orientations of the silicon vacancy center in 4H-SiC, V1 (860 nm) and V2 (916 nm). (b) Representative room temperature PL spectra of nanobeam PCCs coupled to silicon vacancy emission. Upper two spectra (red and blue) are from devices with 320 nm lattice constant, while the rest are from devices with 290 nm lattice constant. (c) Spectra (vertically offset for clarity) taken at 77 K showing the fundamental mode of a nanobeam PCC tuned using laser irradiation to bring the mode into spectral overlap with the V2 ZPL. The measured Q of the mode was 1100. (d) Same as panel c for a second PCC (fundamental mode Q of 1000). A prominent secondary mode is visible at ∼940 nm and tunes along with the fundamental mode. When the fundamental mode and ZPL align, there is a 3-fold intensity increase. (e) Enhanced view of mode and ZPL, featuring blue and green traces from panel d with no offset.

increase in intensity may be due to this change in radiation pattern, the effect of cavity−emitter coupling, and consequent increase in radiative rate into the cavity mode, is apparent. These results indicate that our fabrication and tuning methods show promise for enabling deterministic coupling between photonic devices and quantum emitters in 4H-SiC.

In this work we have demonstrated a method to fabricate nanobeam PCCs using monolithic, homoepitaxially grown 4H-SiC and a dopant-selective PEC etch to create optical isolation. This method produces high-quality factor devices and offers a high yield of successful devices. Such robustness can allow for easy cavity design optimization as well as a high probability of success in finding devices that can couple to the desired emitters. Additionally, we have demonstrated the ability to tune the wavelengths of the resonant modes of these devices, both in bulk and individually. Lastly, we used these methods to couple nanobeam PCC resonant modes to the photoluminescence of silicon vacancy centers and showed that the modes could be tuned to overlap with the ZPL of these centers. Going forward, we will continue to refine our defect implantation methods and optimize our fabrication procedure to create high-quality nanobeam PCCs coupled to the emission of 4H-SiC defect centers. Moreover, we will be able to use the tuning methods reported here in addition to nitrogen condensation tuning, as demonstrated in ref 14. Accordingly, we will be able to achieve even more precise tuning of the PCC modes through resonance with the defect ZPL and, with high-quality devices, seek to characterize Purcell enhancement of the defect emission. Therefore, as this work progresses, the method demonstrated

DOI: 10.1021/acs.nanolett.5b02542
Nano Lett. 2015, 15, 6202−6207

here can be of importance in the development of 4H-SiC as a platform for quantum information.

■ AUTHOR INFORMATION

Corresponding Author

*E-mail: dbracher@fas.harvard.edu.

Notes

The authors declare no competing financial interest.

■ ACKNOWLEDGMENTS

The authors thank D. R. Clarke for access to the confocal Raman microscope, as well as J. Lee and A. Magyar for helpful discussions. The authors acknowledge funding from the Air Force Office of Scientific Research, under the QUMPASS program (Award No. FA9550-12-1-0004). This work was performed in part at the Center for Nanoscale Systems (CNS), a member of the National Nanotechnology Infrastructure Network (NNIN), which is supported by the National Science Foundation under NSF award no. ECS-0335765. CNS is part of Harvard University.

■ REFERENCES

(1) Koehl, W. F.; Buckley, B. B.; Heremans, F. J.; Calusine, G.; Awschalom, D. D. *Nature* **2011**, *479*, 84−87.

(2) Falk, A. L.; Buckley, B. B.; Calusine, G.; Koehl, W. F.; Dobrovitski, V. V.; Politi, A.; Zorman, C. A.; Feng, P. X.-L.; Awschalom, D. D. *Nat. Commun.* **2013**, *4*, 1819.

(3) Widmann, M.; Lee, S. Y.; Rendler, T.; Son, N. T.; Fedder, H.; Paik, S.; Yang, L.-P.; Zhao, N.; Yang, S.; Booker, I.; Denisenko, A.; Jamali, M.; Momenzadeh, S. A.; Gerhardt, I.; Ohshima, T.; Gali, A.; Janzen, E.; Wrachtrup, J. *Nat. Mater.* **2014**, *14*, 164−168.

(4) Hain, T. C.; Fuchs, F.; Soltamov, V. A.; Baranov, P. G.; Astakhov, G. V.; Hertel, T.; Dyakonov, V. *J. Appl. Phys.* **2014**, *115*, 133508.

(5) Castelletto, S.; Johnson, B. C.; Ivády, V.; Stavrias, N.; Umeda, T.; Gali, A.; Ohshima, T. *Nat. Mater.* **2013**, *13*, 151−156.

(6) Kraus, H.; Soltamov, V. A.; Fuchs, F.; Simin, D.; Sperlich, A.; Baranov, P. G.; Astakhov, G. V.; Dyakonov, V. *Sci. Rep.* **2014**, *4*, 5303.

(7) Falk, A. L.; Klimov, P. V.; Buckley, B. B.; Ivády, V.; Abrikosov, I. A.; Calusine, G.; Koehl, W. F.; Gali, A.; Awschalom, D. D. *Phys. Rev. Lett.* **2014**, *112*, 187601.

(8) Weber, J. R.; Koehl, W. F.; Varley, J. B.; Janotti, A.; Buckley, B. B.; Van de Walle, C. G.; Awschalom, D. D. *Proc. Natl. Acad. Sci. U. S. A.* **2010**, *107*, 8513−8518.

(9) Weber, J. R.; Koehl, W. F.; Varley, J. B.; Janotti, A.; Buckley, B. B.; Van de Walle, C. G.; Awschalom, D. D. *J. Appl. Phys.* **2011**, *109*, 102417.

(10) Christle, D. J.; Falk, A. L.; Andrich, P.; Klimov, P. V.; Hassan, J. U.; Son, N. T.; Janzen, E.; Ohshima, T.; Awschalom, D. D. *Nat. Mater.* **2014**, *14*, 160−163.

(11) Faraon, A.; Santori, C.; Huang, Z.; Acosta, V. M.; Beausoleil, R. G. *Phys. Rev. Lett.* **2012**, *109*, 033604.

(12) Hausmann, B. J. M.; Shields, B. J.; Quan, Q.; Chu, Y.; de Leon, N. P.; Evans, R.; Burek, M. J.; Zibrov, A. S.; Markham, M.; Twitchen, D. J.; Park, H.; Lukin, M. D.; Lončar, M. *Nano Lett.* **2013**, *13*, 5791−5796.

(13) Li, L.; Schroder, T.; Chen, E. H.; Walsh, M.; Bayn, I.; Goldstein, J.; Gaathon, O.; Trusheim, M. E.; Lu, M.; Mower, J.; Cotlet, M.; Markham, M. L.; Twitchen, D. J.; Englund, D. *Nat. Commun.* **2015**, *6*, 6173.

(14) Lee, J. C.; Bracher, D. O.; Cui, S.; Ohno, K.; McLellan, C. A.; Zhang, X.; Andrich, P.; Aleman, B.; Russell, K. J.; Magyar, A. P.; Aharonovich, I.; Bleszynski Jayich, A. C.; Awschalom, D. D.; Hu, E. L. *Appl. Phys. Lett.* **2014**, *105*, 261101.

(15) Lu, X.; Lee, J. Y.; Feng, P. X. L.; Lin, Q. *Appl. Phys. Lett.* **2014**, *104*, 181103.

(16) Lu, X.; Lee, J. Y.; Rogers, S.; Lin, Q. *Opt. Express* **2014**, *22*, 30826−30832.

(17) Radulaski, M.; Babinec, T. M.; Müller, K.; Lagoudakis, K. G.; Zhang, J. L.; Buckley, S.; Kelaita, Y. A.; Alassaad, K.; Ferro, G.; Vuckovic, J. *ACS Photonics* **2015**, *2*, 14−19.

(18) Cardenas, J.; Zhang, M.; Phare, C. T.; Shah, S. Y.; Poitras, C. B.; Guha, B.; Lipson, M. *Opt. Express* **2013**, *21*, 16882−16887.

(19) Radulaski, M.; Babinec, T. M.; Buckley, S.; Rundquist, A.; Provine, J.; Alassaad, K.; Ferro, G.; Vučković, J. *Opt. Express* **2013**, *21*, 32623−32629.

(20) Calusine, G.; Politi, A.; Awschalom, D. D. *Appl. Phys. Lett.* **2014**, *105*, 011123.

(21) Lee, J. Y.; Lu, X.; Feng, P. X. L.; Lin, Q. 3C-SiC Nanobeam Optomechanical Crystals. In *OSA Technical Digest*; CLEO: Science and Innovations 2014, San Jose, CA, June 8−13, 2014; SF1M-2.

(22) Song, B. S.; Yamada, S.; Asano, T.; Noda, S. *Opt. Express* **2011**, *19*, 11084−11089.

(23) Yamada, S.; Song, B. S.; Asano, T.; Noda, S. *Appl. Phys. Lett.* **2011**, *99*, 201102.

(24) Yamada, S.; Song, B. S.; Jeon, S.; Upham, J.; Tanaka, Y.; Asano, T.; Noda, S. *Opt. Lett.* **2014**, *39*, 1768−1771.

(25) Magyar, A. P.; Bracher, D.; Lee, J. C.; Aharonovich, I.; Hu, E. L. *Appl. Phys. Lett.* **2014**, *104*, 051109.

(26) Zorman, C. A.; Fleischman, A. J.; Dewa, A. S.; Mehregany, M.; Jacob, C.; Nishino, S.; Pirouz, P. *J. Appl. Phys.* **1995**, *78*, 5136−5138.

(27) Di Cioccio, L.; Le Tiec, Y.; Letertre, F.; Jaussaud, C.; Bruel, M. *Electron. Lett.* **1996**, *32*, 1144−1145.

(28) Purcell, E. M. *Phys. Rev.* **1946**, *69*, 37.

(29) Zhang, Y.; McCutcheon, M. W.; Burgess, I. B.; Loncar, M. *Opt. Lett.* **2009**, *34*, 2694−2696.

(30) Akahane, Y.; Asano, T.; Song, B. S.; Noda, S. *Nature* **2003**, *425* (6961), 944−947.

(31) Castelletto, S.; Johnson, B. C.; Parker, A. *Proc. SPIE* **2013**, *8875*, 88750U.

(32) Korsunska, N. E.; Tarasov, I.; Kushnirenko, V.; Ostapenko, S. *Semicond. Sci. Technol.* **2004**, *19*, 833−838.

(33) Santori, C.; Barclay, P. E.; Fu, K. C.; Beausoleil, R. G.; Spillane, S.; Fisch, M. *Nanotechnology* **2010**, *21*, 274008.

(34) Asano, T.; Song, B. S.; Noda, S. *Opt. Express* **2006**, *14*, 1996−2002.

(35) Michael, C. P.; Srinivasan, K.; Johnson, T. J.; Painter, O.; Lee, K. H.; Hennessy, K.; Kim, H.; Hu, E. *Appl. Phys. Lett.* **2007**, *90*, 051108.

(36) Hennessy, K.; Badolato, A.; Tamboli, A.; Petroff, P. M.; Hu, E.; Atatüre, M.; Dreiser, J.; Imamoğlu, A. *Appl. Phys. Lett.* **2005**, *87*, 021108.

(37) Portalupi, S. L.; Galli, M.; Reardon, C.; Krauss, T.; O'Faolain, L.; Andreani, L. C.; Gerace, D. *Opt. Express* **2010**, *18*, 16064−16073.

DOI: 10.1021/acs.nanolett.5b02542
Nano Lett. 2015, 15, 6202−6207